

Structural and Chemical Modifications of Few-layer Transition Metal Phosphorous Trisulfides by Electron Irradiation

Köster, J.; Storm, A.; Ghorbani Asl, M.; Kretschmer, S.; Gorelik, T. E.; Krasheninnikov, A.; Kaiser, U.;

Originally published:

September 2022

Journal of Physical Chemistry C 126(2022)36, 15446-15455

DOI: <https://doi.org/10.1021/acs.jpcc.2c03800>

Perma-Link to Publication Repository of HZDR:

<https://www.hzdr.de/publications/Publ-35054>

Release of the secondary publication
on the basis of the German Copyright Law § 38 Section 4.

Structural and Chemical Modifications of Few-layer Transition Metal Phosphorous Trisulfides by Electron Irradiation

Janis Köster^{#*1}, Alexander Storm^{*1}, Mahdi Ghorbani-Asl², Silvan Kretschmer², Tatiana E. Gorelik¹, Arkady V. Krashennnikov^{2,3}, and Ute Kaiser^{#1}

¹ Electron Microscopy Group of Materials Science, Ulm University, Albert-Einstein-Allee 11, 89081 Ulm, Germany

² Institute of Ion Beam Physics and Materials Research, Helmholtz-Centre Dresden-Rossendorf, 01328 Dresden, Germany

³Department of Applied Physics, Aalto University, PO Box 14100, 00076 Aalto, Finland

**These authors contributed equally to this work*

Corresponding Author: Janis Köster, janis.koester@uni-ulm.de; Ute Kaiser, ute.kaiser@uni-ulm.de

Abstract - Transition metal phosphorous trisulfides (TMPTs) are inorganic materials with inherent magnetic properties. Due to their layered structure, they can be exfoliated into ultra-thin sheets, which show properties different from their bulk counterparts. Herein, we present a detailed analysis of the interaction of the electron beam (30 – 80 kV) in a transmission electron microscope (TEM) with freestanding few-layer TMPTs, with the aim to tailor their properties. The irradiation-induced structure modifications were systematically investigated by various TEM methods on FePS₃, MnPS₃, and NiPS₃, and the results are rationalized with the help of *ab-initio* calculations, which predict that the knock-on threshold for removing sulfur is significantly lower than that for phosphorus. Therefore, a targeted removal of sulfur is feasible. Eventually, our experiments confirm the dose-dependent, predominantly removal of sulfur by the impinging electrons, thus showing the possibility to tune the sulfur concentration. Using *ab-initio* calculations, we analyze the electronic structure of the TMPTs with single vacancies and oxygen impurities, and predict distinct electronic properties depending on the type of defect. Therefore, our study shows the possibility of tuning the properties of ultrathin freestanding TMPTs by controlling their stoichiometry.

1. INTRODUCTION

Two-dimensional (2D) materials exhibit a variety of intriguing electronic, optical, and magnetic properties^{1–4}. Moreover, by combining individual layers^{5,6}, heterostructures with unique characteristics can be designed^{5,7–10}. One promising class of 2D materials with interesting properties is transition metal phosphorous trichalcogenides^{11–13} (TMPTs). They show a large variety in band gaps,^{14,15} ranging from 1.5 eV to 3.0 eV^{16,17}, and the chemical elements they consist of are largely earth abundant and nontoxic¹⁸, which makes them suitable candidates for optoelectronic applications^{19,20}. Specifically, TMPTs show inherent magnetic properties. They belong to the recently investigated antiferromagnetic 2D materials^{21–23}, as the magnetism persists down to the few-layer limit^{24,25}, suggesting them as testbeds for studying the fundamental aspects of 2D magnetism^{18,26}. Moreover, the layered structure of TMPTs makes few-layer and bulk systems excellent candidates for intercalation by ions or molecules. Consequently, they are suitable

materials also for energy storage^{27–30,31}. In particular, due to the high binding energy of Li to their surface, applications of TMPTs as anode materials in Li-ion batteries have already been predicted^{32,33}.

First theoretical and experimental studies showed the possibility of tailoring the properties of these materials. As an example, cooperative spin-crossovers and semiconductor-to-metal transitions were observed in MnPS_3 and MnPSe_3 under high pressure³⁴. At the same time, TMPTs have not yet been intensively analyzed experimentally to understand defect-induced properties, although the theoretical studies on single-layers predicted intriguing defect-induced changes in the electronic and magnetic properties of the materials, e.g. the inclusion of spin-split mid-gap states in MnPS_3 ³⁵. Furthermore, in several studies^{36–38} stacking faults were reported for various bulk TMPTs, and it was shown that the properties (i.e. thermal conductivity) of the materials are strongly altered by these defects^{39,40}, however, no detailed studies on the effect of these faults on few-layer systems are given in the literature.

Transmission electron microscopy (TEM) is a particularly useful tool for probing^{41–44}, modifying and tailoring^{45–49} the properties of freestanding nanosheets with energetic electrons. This technique allows gaining chemical and crystallographic information from the materials, which can be correlated with each other even on an atomic scale using aberration-corrected (AC) high-resolution (HR) TEM^{50–52}. A necessary condition is the preparation of pristine clean freestanding few-layer TMPTs samples, which recently was succeeded via polymer-assisted mechanical exfoliation⁵³. However, detailed experimental analysis and characterization of the interaction of energetic electrons in low-voltage (30 - 80 kV) TEM with the ultra-thin TMPT is still missing.

In this work, we study the response of freestanding few-layer TMPTs to the electron beam at acceleration voltages in the range of 30 - 80 kV. Structural changes associated with chemical and electronic properties were studied in spherical and chromatic aberration-corrected HRTEM, electron diffraction (ED), energy-dispersive X-ray spectroscopy (EDX) and time-dependent electron energy loss spectroscopy (EELS). Experimental results were rationalized with the help of *ab-initio* calculations, and damage cross-sections were assessed using the McKinley-Feshbach formalism. In addition, the effects of defects on the electronic properties of the irradiated materials were studied.

2. METHODS SECTION:

Materials: Thin flakes of TMPTs were prepared by a polymer-assisted sample preparation method based on mechanical exfoliation. Bulk crystals were thinned down by exfoliation via an adhesive tape and pressed onto a polyvinyl acetate coated silicon substrate. The underlying polymer layer allows a gentle transfer with distilled water of the thin flakes to a Quantifoil TEM grid⁵³. Samples prepared in this way were thin and clean freestanding flakes, and could directly be used for TEM investigations.

TEM Experiments: HRTEM and EELS experiments were conducted at the Cc/Cs-corrected Sub-Ångström Low Voltage Electron Microscope (SALVE) at 30 - 80 kV. The energy resolution in the EELS experiments was determined to be 0.65 eV from the full width at half maximum of the zero-loss peak, measured in

vacuum. If not stated otherwise, for all presented core-loss EELS signals in the spectra, the background was removed with the help of the power-law model⁵⁴, which has shown to give good results in previous analyses of elemental core-loss edges^{55–57}. Following the method for quantification of ferrous/ferric ratios in the $M_{2,3}$ edges proposed by van Aken⁵⁸, the change of the valence in Fe is determined by the intensity ratio of the main to the pre-peak in the Fe $M_{2,3}$ edge. Therefore, two integration windows of 2.5 eV one around the main peak w_M and a second one w_P directly in front of the other window are acquired and the ratio $\left(\frac{w_M}{w_P}\right)$ of both is evaluated. The second method to evaluate the valence composition of an iron bearing compound is the determination of the white line ratio of the Fe $L_{2,3}$ edge^{55,56,59,60}. Here, the method for quantification of ferrous/ferric ratios in the $L_{2,3}$ edges proposed by van Aken et al.⁵⁶ was adapted. On the background subtracted spectra a double arctan function with inflection points at the minima behind the two main peaks is fitted and subtracted to remove excitations to the continuum for each spectrum respectively. In the next step, two integration windows of energy width 2 eV with the first (w_{L_3}) centered around 709.5 eV, the maximum of the L_3 edge of the last acquired spectrum (irradiated), and the second (w_{L_2}) at 720.9 eV, the maximum of the L_2 edge of the pristine structure, are applied. Then the ratio $\left(\frac{w_{L_3}}{w_{L_2}}\right)$ is evaluated.

HRTEM image simulations were performed using the open source *abTEM* Python Application Programming Interface based on the multislice algorithm⁶¹ and the effect of finite electron dose was included via addition of noise, using the Poisson statistics⁶². The energy-dispersive X-ray spectroscopy (EDX) experiments were conducted at a Talos F200X G2 STEM. Peaks are fitted to the acquired EDX spectrum for the selected elements, and the atomic fractions are calculated with the help of the Brown-Powell model⁶³ to determine the elemental composition.

Electron diffraction data (ED) were collected using a TITAN TEM operated at 300 kV in nanodiffraction mode with a condenser C2 aperture of 50 μm and an effective beam diameter on the sample of 1 μm . The data were collected at room temperature using a Fischione Advanced Tomo Holder 2020 and a Gatan US1000-XP 2k CCD camera. Tilt series were collected using a dedicated Digital Micrograph script⁶⁴. The data were processed using PETS2 software⁶⁵, supported by home-written MATLAB scripts.

Computational Methods: The energetics and electronic structure of all point defects were investigated using spin-polarized density functional theory (DFT) as implemented in the VASP code^{66,67}. All the calculations were carried out using the PBE exchange-correlation functional⁶⁸. The primitive cells were fully optimized with an energy cut-off of 600 eV and a force tolerance of 0.01 eV \AA^{-1} . The point defects were modeled using a 3x2x1 supercell with a vacuum space of 20 \AA in the confinement direction. The Brillouin zone of the systems was sampled using 8x8x1 Monkhorst-Pack grid for primitive cells and 3x3x1 for supercells. In the electronic structure calculations, the DFT + U method with an effective Hubbard value (U) of 5.5 eV for transition-metal atoms was employed.

The formation energies E_f of vacancies (chemical element X) were computed as $E_f = E_{vacancy} - E_{pristine} + \mu_x$, where $E_{vacancy}$ and $E_{pristine}$ are the energies of the defective and pristine supercell, respectively. μ_x represents the chemical potential of the X species, which is considered to be the energy of the isolated atom.

Ab-initio molecular dynamics as implemented in the VASP package was used to simulate the displacement process (spin-polarized calculations with Hubbard term, plane wave cutoff 400 eV, k-points according to Monkhorst-Pack 3x3x1, time step 0.2 fs). An initial velocity was assigned to the recoil atom in the direction normal to the surface, for non-normal displacements an inclination of 30° relative to the surface normal was chosen. In the simulations, the initial velocity was increased until the atom meets the displacement criteria (minimum 5 Å displacement, force on atom < 0.1 eV/Å).

3. RESULTS

3.1 Crystal structure and thickness analysis: We start our study by analyzing the orientation, flake thickness, and quality of the transferred pristine few-layer material, see Figure 1 (a), which is known to be prone to oxidation⁵³. Since MnPS₃, FePS₃ and NiPS₃ are isostructural, all structural considerations presented in the following for MnPS₃ are valid for all three materials.

In bulk MnPS₃, the layers are stacked in a shifted manner, obeying the monoclinic symmetry⁶⁹ with $\beta = 107^\circ$ (Figure 1 (b)). [103] is the normal vector to the layer plane and is denoted here as *normal incidence*, as it is the observed orientation in all presented HRTEM results (Figure 1 (c)). In this projection, the structure has a rectangular centered pattern with a pronounced hexagonal pseudo symmetry, and the unit cell contains 6 atomic rows along **b** vector (marked in Figure 1 (b)) with different atomic compositions: rows 1 and 4 consist of S and P atoms, rows 2, 3, 5, 6 consist of S and Mn atoms, resulting in a 1:2 rows alteration, depicted in (c). Our detailed ED study (see *supporting information (SI) section 1*), shows that the prepared few-layer flakes exhibit no stacking faults.

In addition, we performed multislice image simulations to understand the intensity differences of mono- to 6-layers in the [103] orientation (see *SI section 2*). In Figure 1 (c) a 4-layer crystal with absent stacking faults shows the best match to the experimental image, and the good crystallinity of these thin samples can be appreciated. Line scans besides, illustrate the 1:2 alternation mentioned above. An alternative TEM method for thickness determination⁷⁰ gives a thickness value of around 3 nm, which reassures the finding of the image simulation, see *SI section 3*. Therefore, we conclude that the analyzed pristine samples are few-layer systems, 3 - 6 layers, of good sample quality, without stacking faults.

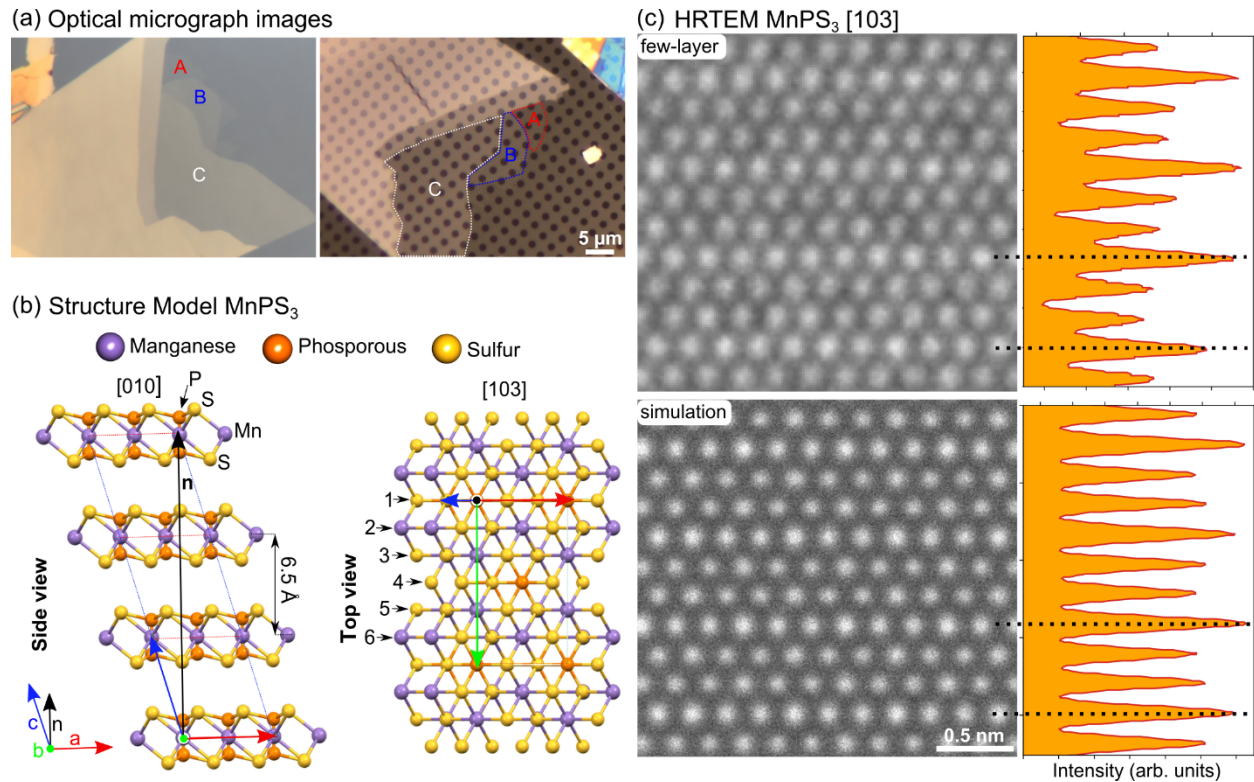


Figure 1. (a) Optical micrograph images of MnPS₃ on a polyvinyl acetate coated silicon substrate (left inset) and transferred to a TEM Quantifoil grid (right inset). Three flakes with different number of layers are highlighted by colored letters. (b) Structure models illustrating the stacking order in MnPS₃ - side view and top view along the [103] direction of the bulk structure. The unit cell is indicated by colored arrows in which the normal *n* is shown in black. (c) Cc/Cs-corrected High-resolution TEM image of MnPS₃ recorded at 80 kV and a simulated one of a four-layer model without stacking faults.

3.2 Electron-specimen interaction: Continuous irradiation of the sample leads to degradation of individual layers. An example showing a 4-layer sample from pristine to degraded, including patches of 1-3 layers, can be found in Figure S5. In this context, individual defects in the layers can be observed. Figure 2 (a,b) display 80 kV HRTEM images of a NiPS₃ single- and double-layer, respectively, showing distinct defects, highlighted by white arrows. The contrast at the defect sight in the double-layer vanishes as seen from the inset in (b), showing a red line-scan obtained from the area marked by a red rectangular. The defect shows a sulfur (S) vacancy (*V_S*) in an atom column in which two S atoms of the two layers are located above each other (*S₂*).

Understanding the formation of single defects pave the way to explore the response of these layered systems to the electron irradiation in TEM, and to systematically modify the system's properties. Our TEM experiments indicate that sulfur or phosphorus vacancies first emerge, which then lead to larger defects or even holes in the layer. Formation energies for phosphorus and sulfur vacancies and the corresponding displacement energies (*T_d*) in single-layer TMPTs are obtained from ab-initio molecular dynamics simulations (Figure 2 (c)). *T_d* is determined as the minimum kinetic energy that must be assigned to the recoil atom so that it leaves its position from the crystal without immediate recombination.

For normal displacement (that is the direction of the initial velocity vector being perpendicular to the surface), the recoil sulfur atom pulls the closest phosphorus atom behind, which leads to the displacement of a phosphorus-sulfur dumbbell (S-P). Displacement deviating from the surface normal, e.g. under a slight deviation of the electron beam from the normal direction, is required to remove single sulfur atoms (S^* , denotes non-normal displacement).

Furthermore, the atom displacement cross-section was estimated by using the McKinley-Feshbach formalism^{50,71–73}. For an accurate estimation of lattice vibrations on the cross-section the Debye-Temperature (θ_D) model was employed as described in detail in *SI section 5*. Figure 2 (d) presents the cross-sections for knock-on displacements of S and P atoms in $FePS_3$, $MnPS_3$ and $NiPS_3$ ^{50,71,74,75}. In addition, the knock-on cross-section for graphene is shown for comparison, indicating a considerably higher threshold. Overall, the displacement threshold for sulfur is significantly lower than for phosphorous. As a result, it can be predicted that more S should be removed than P due to elastic interaction in the acceleration voltage range of 50 - 300 kV. It has been known that inelastic damage plays a significant role in 2D insulators and semiconductors^{75,76}. Such additional channels for defect production were shown to be important for the formation of single S vacancies in MoS_2 single-layer⁷⁶ where damage production was observed for the electron energies well below the knock-on threshold. Therefore, considering inelastic effects and the fact that S is three times more abundant in the initial structure, it can be expected that S is easily removed by the high energy electrons (20 - 300 kV) in single-layer TMPTs. In few-layer systems, strong structural modifications due to electron interactions can be also expected and are experimentally evaluated in the following sections.

In order to elaborate the effects of defects on the electronic properties, the atomic structure of the pristine material was first calculated and the optimized lattice constants (see Table 1) proved to be in very good agreement with the experimental values and the previous theoretical reports¹⁸. Then the spin-polarized density of states (DOS) was calculated, which is shown in Figure 3. Our results indicate that TMPT single-layers have a semiconductor character with a bandgap in the range of 2.0 - 2.3 eV. Even though the DFT band gap should not be directly compared⁷⁷ to the optical gap measured in the experiment, our band gap, calculated at the PBE+U level, for $FePS_3$ single-layer is consistent with the experimental value of 2.2 eV¹⁷.

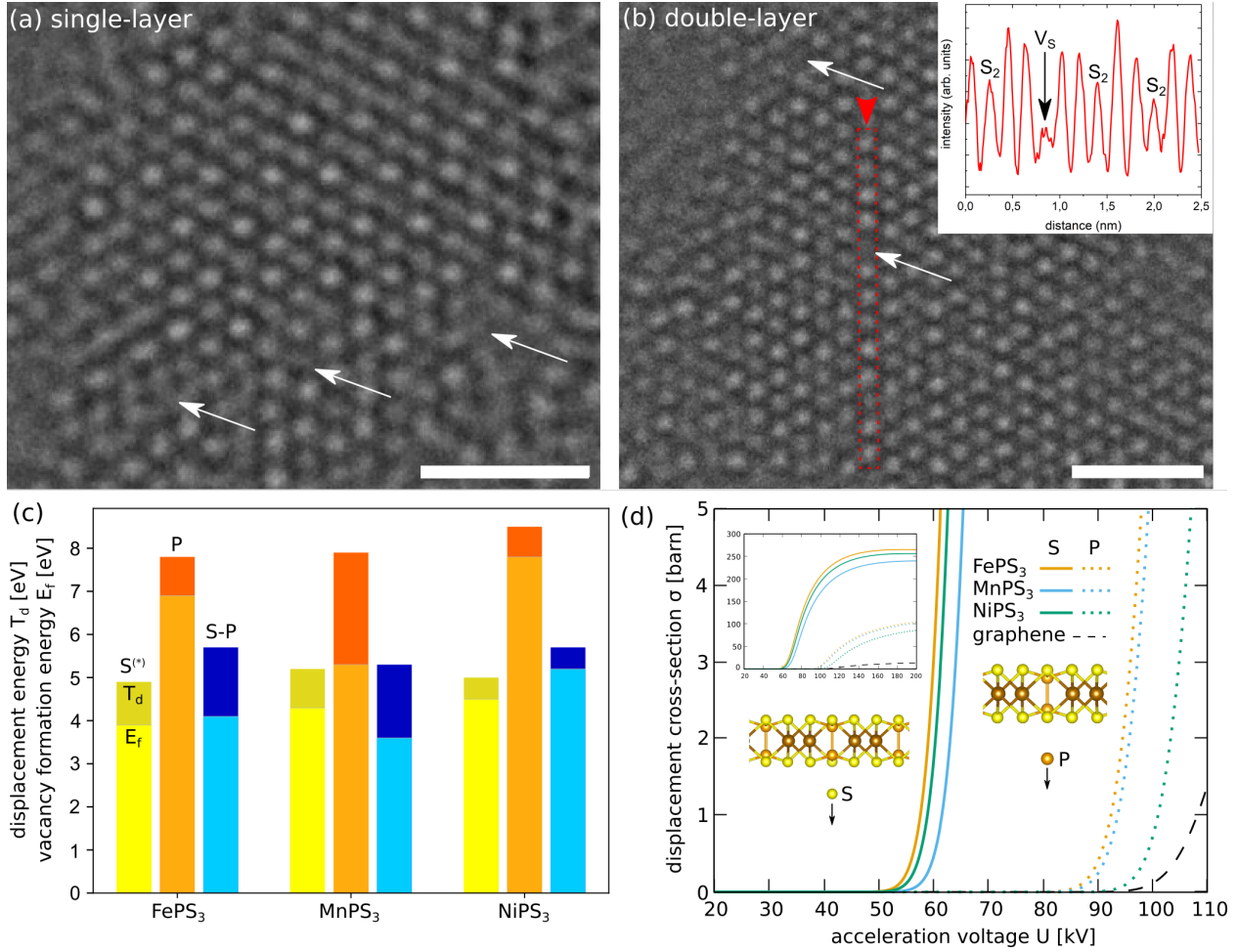


Figure 2. (a,b) 80 kV Cc/Cs-corrected HRTEM images of single- and double-layer NiPS₃, respectively. White arrows mark selected isolated vacancies. In (b), a line scan over a S vacancy site (V_s) in the double-layer system is depicted as an inset, obtained from the red dashed area. Scale bars represents 1 nm. (c) Displacement energies T_d and defect formation energies E_f for FePS₃, MnPS₃, NiPS₃. Single S atom sputtering appears only under a slight deviation of the initial velocity vector from the surface normal (S^{*}). For normal displacement the S atom pulls the P atom behind, forming a S-P dumbbell. (d) Damage cross-sections over the acceleration voltage for FePS₃, MnPS₃, NiPS₃; and graphene as a reference (black dashed curve). Cross-sections are calculated by the McKinley-Feshbach formalism with account for lattice vibrations (Debye model). Solid curves represent the sulfur displacement, dotted curves the phosphorus displacement cross-section. The inset displays the cross-sections up to 200 kV.

Table 1. Experimental and calculated single-layer lattice constants (*a*) and layer thickness (*d*) of TMPTs (AFM denotes antiferromagnetic).

	<i>a</i> (Å)		<i>d</i> (Å)	Magnetic character
	exp.	DFT	DFT	Antiferromagnetic (AFM)
MnPS ₃	6.07 ⁶⁹	6.05	3.23	Néel
FePS ₃	5.95 ⁶⁹	5.87	3.13	zigzag
NiPS ₃	5.81 ⁶⁹	5.82	3.03	zigzag

Furthermore, we considered three types of point defects, sulfur and phosphorus vacancies (V_S and V_P) and a complex vacancy corresponding to sulfur and phosphorus (V_{SP}) missing atoms. The presence of sulfur vacancy introduces new spin-polarized states close to the conduction and valence band edges, which are mainly contributed by S-p orbitals. The exception is $MnPS_3$, where the defect states are formed as part of the band continuum. In the case of a single P vacancy, new localized states are formed 0.2 - 0.7 eV above the conduction band edge. Defect-associated states are clearly more pronounced in the case of V_{SP} , where the electron density is increased around the Fermi level particularly for $FePS_3$.

3.3 Electron beam stimulated chemical and structural modification analyzed by EELS and EDX:

Here, $FePS_3$ is presented in detail and unless noted otherwise, analogous behavior was found for the corresponding Mn and Ni bearing components (see *SI sections 6 and 7*). Figure 4 shows an 80 kV HAADF image and elemental maps of irradiated and pristine samples. A disordering and formation of clusters can be observed in the irradiated areas, see the magnified area in Figure 4 (a) and Figure S12. The comparison of the atomic fractions in the pristine and irradiated regions reveals that mostly S is removed, which coincides well with our theoretical results (Figure 4 (b,c)).

To further facilitate a comparison with the experimental results, we modeled phases with intermediate stoichiometry, which can potentially form in the sulfur-deficient material. The phases were generated by a uniform increase of vacancies in the pristine structure, simulating the experimental conditions under prolonged electron irradiation. For high concentrations of S vacancies (>50%), the optimized structures of the phases revealed metal atom clustering similar to our experimental data. Such non-stoichiometric phases can be stabilized in the metal-rich limit as shown before for transition-metal dichalcogenides⁷⁸. The electronic structures were also analyzed for different concentrations of S vacancies. As expected, the number of midgap states increases with defect concentration. However, we found out that the position of the states depends on the distribution of defects. Eventually the states are expected to fill the whole band gap region indicating that the irradiated samples may exhibit hopping-type conductivity.

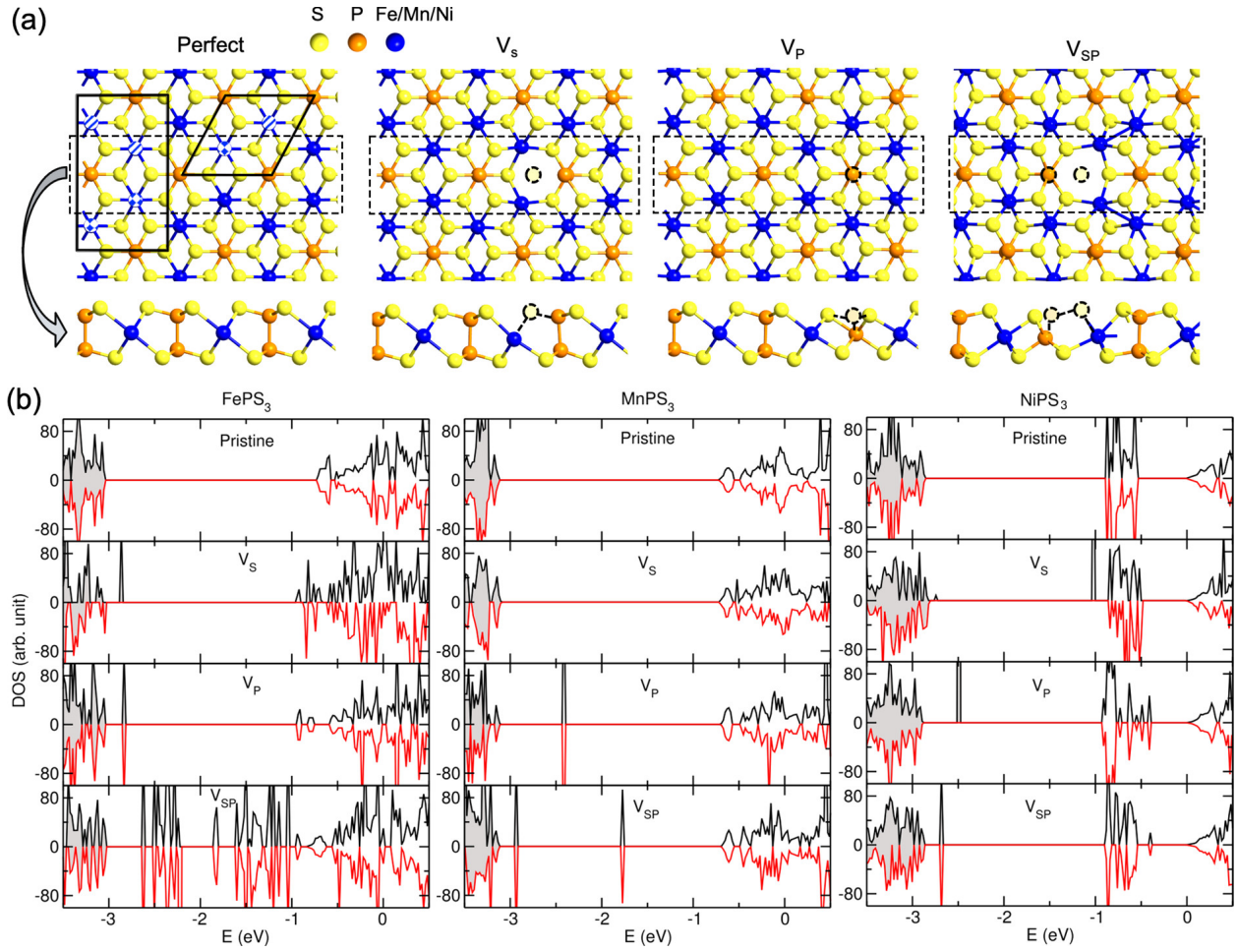


Figure 3. (a) Atomic structures of single S* and P and S-P vacancies in single-layer TMPTs. The solid black lines indicate unit cells of the systems with zigzag and Néel antiferromagnetic order, respectively. The hatched blue markers represent the directions of local spins (spin-up: checkerboard, spin-down: striped). (b) Spin-polarized total densities of states for various point defects in TMPTs. The spin-up and spin-down components are shown in black and red. The occupied states are filled (grey). The band structures are aligned in such a way that the valence band maximum (extended states not associated with defects are at the same position).

Further, after irradiation, an increase in oxygen content is detected, and both observed effects become more prominent for strongly irradiated regions. The presence of oxygen as a substitutional impurity modifies the electronic structure of the FePS₃ system by creating new levels in the middle of the gap. The results are added to Figure S13. It is evident that although the positions of the defect-induced states in the gap change, the deep states do not completely disappear.

The transformation process (Figure 5 (a)) is analyzed with the help of ELNES in the corresponding core-loss EELS edges, as described in the Method section, and the change of the microstructure is presented in *SI section 8*. For this purpose, EELS signals were acquired over time with constant low electron dose (dose rate of $15 \times 10^3 \text{ e}^-/(\text{s} \cdot \text{nm}^2)$), and the corresponding changes in the ELNES of the materials were identified, and the evolution of the spectrum over the acquisition time is displayed in Figure 5.

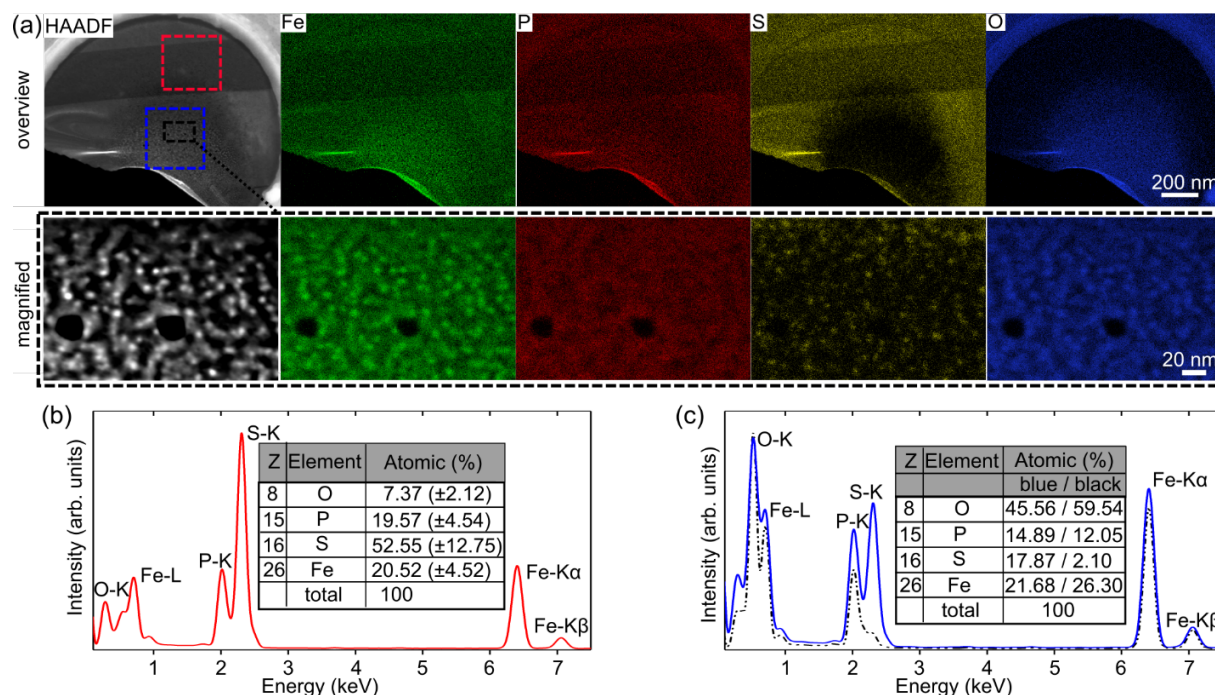


Figure 4. HAADF image of a few-layer FePS₃ flake and corresponding elemental maps of Fe, P, S and O are shown in (a). Upper row: Overview data. The irradiated region is marked by the dashed blue rectangular and a pristine region in red in the HAADF image. Lower row: Magnified data framed with black dotted border from the blue marked region in the overview HAADF image in the upper row. (b), (c) Corresponding energy dispersive EDX profiles for the pristine (b) and irradiated (c) regions. In (c), the black dotted curve corresponds to the magnified data. Elemental quantifications are presented in tables as insets in the diagrams. Two values are given for the irradiated area. The first column, values of the blue and the second column represents the black dotted curve.

In Figure 5 (b), the Fe M_{2,3} edge of few-layer FePS₃ is shown for different acquisition times. The M_{2,3} edge of first row transition metals have been used to identify the oxidation state of the corresponding transition metal in a compound^{58,79}. The spectrum of a divalent iron (Fe²⁺) is given by a prominent pre-peak and a broad maximum at around 57 eV⁵⁸. With a change from divalent to ferric iron (Fe³⁺), the main peak blue shifts and the intensity of the pre-peak decreases^{58,79}. The EELS signal of the M_{2,3} edge of pristine few-layer FePS₃ corresponds to a spectrum of mainly divalent iron, which is in good agreement with the proposed valence of iron in this material^{80,81}. By increasing exposure time, a blue shift of the main peak and a strong decrease of the intensity of the pre-peak is observed in the spectrum. The decrease of the pre-peak can be more clearly seen in Figure 5 (c), where the maximum is aligned to 56.9 eV for each spectrum, respectively. The intensity ratio of the main to the pre-peak $\frac{w_M}{w_P}$ (Figure 5 (d)) changes from 1.7 (pristine) to around 2.8 (irradiated) suggesting a transition from divalent to ferric iron⁵⁸. Nevertheless, an absolute determination of the ferric to divalent iron concentration is not given as the derived universal curve⁵⁸ was only proposed for valence calibrated iron oxides in the high-spin configuration and general unambiguous quantification of the valence with the help of the intensity ratio is difficult^{57,82}.

Figure 5 (e) shows the core-loss EELS of the Fe $L_{2,3}$ edge, and the integral ratio $\frac{w_{L_3}}{w_{L_2}}$ of the white line areas (L_3 to L_2) is presented in (f). The blue shift of the main L_3 peak and the increase of the $\frac{w_{L_3}}{w_{L_2}}$ ratio for the irradiated sample prove the gradual change of the valence^{55,56,59,60} from Fe^{2+} to Fe^{3+} and confirms the results obtained from the $M_{2,3}$ edge.

In the case of the $L_{2,3}$ P-S edge, onsets of the P and S edges are highlighted by a distinct peak at around 132 eV (I) and a small peak at slightly higher energy 138.5 eV (II), respectively (see Figure 5 (g)). The former peak is in good agreement with previously reported results obtained with XPS²³ and can be attributed to a combined peak of P- $2p_{1/2}$ and P- $2p_{3/2}$ transitions to $3s \sigma^*$ due to S-P bonding^{23,83}. The same holds true for the peak observed at 162 eV at the pristine structure, which originates from the S- $2p_{1/2}$ and S- $2p_{3/2}$ transitions^{23,83}. With increasing time and interaction with the electron beam, the P-peak at 132 eV decreases (i.e. P-S bond is broken) and eventually two peaks at 138.5 eV (II) and 146.5 eV (III) arise. In addition, the peaks stemming from the phosphor contributions become more prominent in the normalized spectra in comparison to the sulfur contributions. This is in good agreement with the theoretical analysis suggesting that mainly sulfur atoms are removed from the sample under the electron beam.

Figure 5 (h, i) shows the raw and the extracted signal of the O-K edge sequentially acquired to the other presented spectra. Under the prolonged exposure time, the oxygen edge becomes more pronounced indicating higher oxygen concentration in the illuminated area. The source of oxygen stems from two main factors, firstly the residual surface contamination, and secondly the imperfect vacuum in the TEM chamber, discussed in detail in *SI section 9*. This is in line with the EDX results, which show a large oxygen fraction of the illuminated area in comparison to the unaltered flake, Figure 4.

The arising peaks at 138.5 eV and 146.5 eV at the $L_{2,3}$ P edge fit well with previous reports on P-O bonds in oxidized P bearing materials^{84–86} and they suggest that the accumulated oxygen bounds to the residual phosphorus. Also, the combination of the EELS experiments (Figure 5) exhibiting the shift of the valence of Fe^{2+} to Fe^{3+} with EDX results (Figure 4) confirm the bounding between O and Fe. Nevertheless, unambiguous identification of the local chemical (i.e. stoichiometry) and structural composition of the oxidized structure after the electron beam interaction is not feasible.

Similar results are obtained for 30 kV and 60 kV irradiation experiments, which are presented and discussed in detail for $MnPS_3$ in *SI section 10*.

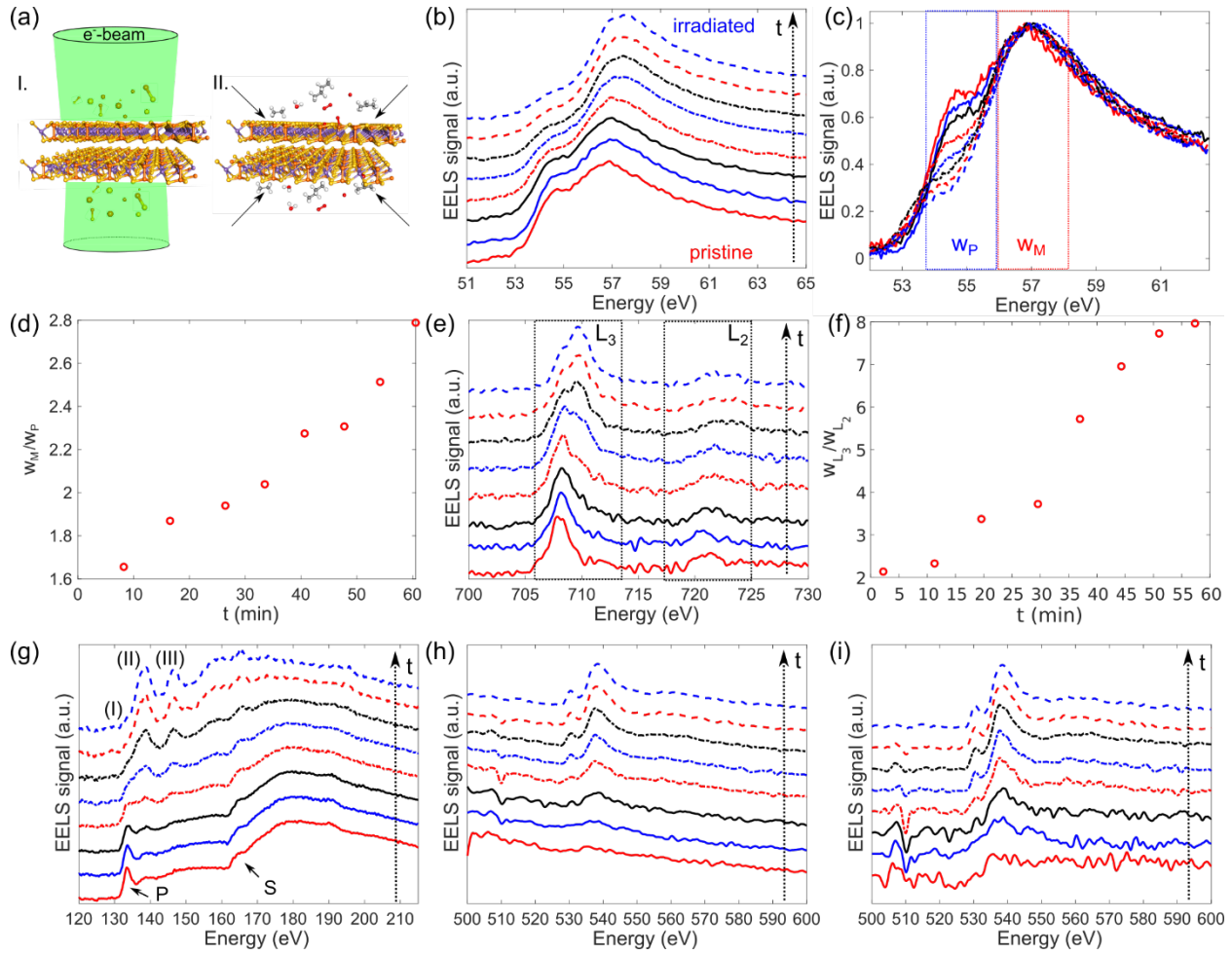


Figure 5. Core-loss EELS analysis of few-layer FePS₃ acquired over time under constant electron irradiation with a dose rate of $15 \times 10^3 \text{ e}^-/(\text{s} \cdot \text{nm}^2)$. (a) Sketch of the transformation process caused by the interaction of the material with the impinging electrons. (b) Evolution of the Fe M_{2,3} edge over time from pristine (red solid line) to irradiated sample (blue). Strong changes in the edge can be appreciated with a blue shift of the M₂ peak (around 57 eV) and a decrease of the pre-peak. (c) the same spectra as in (b), but centered for the main peak around 56.9 eV, the determined maximum of the pristine structure, are shown. (d) change of the intensity ratio of the main to the pre-peak over time (60 min) calculated for the centered peaks of (c). The details of the integration methodology are given in the main EELS part. Changes of the Fe L_{2,3} edge over time (same time ordering as in (b)) are given in (e). A strong shift of the L₃ edge to higher energies can be observed. The corresponding white-line ratios of the L₃ to the L₂ for the different acquisition times are given in (f). A strong increase due to the interaction of the material with the electron beam can be appreciated. The overlapping L_{2,3} edges of S and P over time are given in (g). Strong changes in the ELNES of the P L_{2,3} edge can be observed as well as a reduction of the S contributions. The corresponding signal of the O-K edge over time are presented as raw spectrum (h) and extracted spectrum (i).

4. Conclusion

In this study, we systematically addressed the structural and chemical modifications of few-layer MnPS₃, FePS₃, and NiPS₃ by 30 to 80 keV electrons in the spherical and chromatic aberration-corrected low-voltage SALVE microscope. Starting with a detailed TEM analysis of pristine exfoliated material we showed that the investigated transferred materials are few-layer samples of good crystal quality. Subsequently, we

observed that single vacancies are produced in the pristine material due to the interaction with the electron beam.

Our first-principles calculations predict significantly lower knock-on thresholds for ternary TMPTs as compared to graphene and many binary TMDs. Specifically, sulfur atoms have the lowest knock-on threshold leading to their predominant removal from these atomically thin materials. Single sulfur vacancies introduce defect-associated new states in the bandgap, and depending on sulfur concentration magnetic properties due to asymmetric spin polarization emerge. Furthermore, extended defects produce more pronounced states close to the conduction and valence band edges, for instance S-P dumbbell vacancies in FePS₃ strongly increase the electron density around the Fermi level.

In the TEM, EELS and EDX experiments were carried out for all the studied TMPTs, which illustrate the predicted strong modifications, and clearly show the possibility to change the sulfur concentration caused by the interaction with the probing electrons in the materials. Furthermore, ELNES analysis of M and L edges reveal that after defect formation subsequently O is drawn towards the sample, and that the residual P, as well as transition metal oxidize, illustrating the sensitivity of TMPTs to oxidation, and the necessity to control the imaging conditions (i.e. dose-rate as well as the irradiation time). Overall, our systematic study lays the foundation for investigating and tailoring the electronic and structural properties of freestanding few-layer TMPTs by the TEM's probing electrons.

Supporting Information

A detailed analysis of the hexagonal pseudo symmetry in normal incidence, exemplified by the experimental and simulated electron diffraction pattern. Image simulations of different layer systems. $\frac{t}{\lambda}$ log-ratio method to show the thickness of the analyzed crystals. HRTEM image analysis of irradiated NiPS₃. Derivation of the knock-on thresholds within the McKinley-Feshbach formalism based on the inclusion of lattice vibrations. Additional 80 kV EDX and EELS results for MnPS₃ and NiPS₃, as well as experimental EELS results for 30 kV and 60 kV of MnPS₃. Additional HRTEM image series of few-layer FePS₃. Spin-polarized total densities of states calculation for substitutional doping with O atoms. TEM analysis of the origin of the observed Oxygen accumulation.

ACKNOWLEDGMENTS

We want to thank all cooperation associates in the framework of this manuscript. Further, we especially thank the Institute Laue-Langevin, for the syntheses of the TMPT materials used in this work. We thank Gabriele Es-Samlaoui for successfully preparing the samples for TEM investigation. Further, we thank Hannu Pekka-Komsa for the fruitful discussions on Debye temperatures in TMPTs. This work is supported by a project funded by Carl Zeiss foundation. The computational support from the Technical University of Dresden computing cluster (TAURUS) and High-Performance Computing Center (HLRS) in Stuttgart is gratefully appreciated. We further thank the German Research Foundation (DFG) through projects KR

4866/8-1, the collaborative research center “Chemistry of Synthetic 2D Materials” CRC-1415-417590517 and the collaborative research center “Exploiting the Human Peptidome for Novel Antimicrobial and Anticancer Agents” CRC-1279-316249678 for financial support.

REFERENCES

- (1) Tang, K.; Qi, W.; Li, Y.; Wang, T. Electronic Properties of van Der Waals Heterostructure of Black Phosphorus and MoS₂. *J. Phys. Chem. C* **2018**, *122* (12), 7027–7032.
- (2) Chowdhury, T.; Sadler, E. C.; Kempa, T. J. Progress and Prospects in Transition-Metal Dichalcogenide Research beyond 2D. *Chem. Rev.* **2020**, *120* (22), 12563–12591.
- (3) Zhao, B.; Shen, D.; Zhang, Z.; Lu, P.; Hossain, M.; Li, J.; Li, B.; Duan, X. 2D Metallic Transition-Metal Dichalcogenides: Structures, Synthesis, Properties, and Applications. *Adv. Funct. Mater.* **2021**, *31* (48), 2105132.
- (4) Gong, C.; Zhang, Y.; Chen, W.; Chu, J.; Lei, T.; Pu, J.; Dai, L.; Wu, C.; Cheng, Y.; Zhai, T.; et al. Electronic and Optoelectronic Applications Based on 2D Novel Anisotropic Transition Metal Dichalcogenides. *Adv. Sci.* **2017**, *4* (12), 1700231.
- (5) Geim, A. K.; Grigorieva, I. V. Van Der Waals Heterostructures. *Nature* **2013**, *499* (7459), 419–425.
- (6) Zhang, S.; Liu, J.; Kirchner, M. M.; Wang, H.; Ren, Y.; Lei, W. Two-Dimensional Heterostructures and Their Device Applications: Progress, Challenges and Opportunities—Review. *J. Phys. D. Appl. Phys.* **2021**, *54* (43), 433001.
- (7) Choi, W.; Choudhary, N.; Han, G. H.; Park, J.; Akinwande, D.; Lee, Y. H. Recent Development of Two-Dimensional Transition Metal Dichalcogenides and Their Applications. *Mater. Today* **2017**, *20* (3), 116–130.
- (8) Gao, L. Flexible Device Applications of 2D Semiconductors. *Small* **2017**, *13* (35), 1603994.
- (9) Pataniya, P. M.; Sumesh, C. K. WS₂ Nanosheet/Graphene Heterostructures for Paper-Based Flexible Photodetectors. *ACS Appl. Nano Mater.* **2020**, *3* (7), 6935–6944.
- (10) Li, L.; Shang, Y.; Lv, S.; Li, Y.; Fang, Y.; Li, H. Flexible and Highly Responsive Photodetectors Based on Heterostructures of MoS₂ and All-Carbon Transistors. *Nanotechnology* **2021**, *32* (31), 315209.
- (11) Ressouche, E.; Loire, M.; Simonet, V.; Ballou, R.; Stunault, A.; Wildes, A. Magnetoelectric MnPS₃ as a Candidate for Ferrotoroidicity. *Phys. Rev. B - Condens. Matter Mater. Phys.* **2010**, *82* (10), 100408.
- (12) Wildes, A. R.; Rule, K. C.; Bewley, R. I.; Enderle, M.; Hicks, T. J. The Magnon Dynamics and Spin Exchange Parameters of FePS₃. *J. Phys. Condens. Matter* **2012**, *24* (41), 416004.
- (13) Liu, J.; Li, X. B.; Wang, D.; Lau, W. M.; Peng, P.; Liu, L. M. Diverse and Tunable Electronic Structures of Single-Layer Metal Phosphorus Trichalcogenides for Photocatalytic Water Splitting. *J. Chem. Phys.* **2014**, *140* (5), 054707.
- (14) Ismail, N.; Temerk, Y. M.; El-Meligi, A. A.; Badr, M. A.; Madian, M. Synthesis and Characterization of MnPS₃ for Hydrogen Sorption. *J. Solid State Chem.* **2010**, *183* (5), 984–987.

- (15) Ismail, N.; El-Meligi, A. A.; Temerk, Y. M.; Madian, M. Synthesis and Characterization of Layered FePS₃ for Hydrogen Uptake. *Int. J. Hydrogen Energy* **2010**, 35 (15), 7827–7834.
- (16) Du, K. Z.; Wang, X. Z.; Liu, Y.; Hu, P.; Utama, M. I. B.; Gan, C. K.; Xiong, Q.; Kloc, C. Weak Van Der Waals Stacking, Wide-Range Band Gap, and Raman Study on Ultrathin Layers of Metal Phosphorus Trichalcogenides. *ACS Nano* **2016**, 10 (2), 1738–1743.
- (17) Zhang, X.; Zhao, X.; Wu, D.; Jing, Y.; Zhou, Z. MnPSe₃ Monolayer: A Promising 2D Visible-Light Photohydrolytic Catalyst with High Carrier Mobility. *Adv. Sci.* **2016**, 3 (10), 1600062.
- (18) Hashemi, A.; Komsa, H. P.; Puska, M.; Krasheninnikov, A. V. Vibrational Properties of Metal Phosphorus Trichalcogenides from First-Principles Calculations. *J. Phys. Chem. C* **2017**, 121 (48), 27207–27217.
- (19) Gao, T.; Zhang, Q.; Li, L.; Zhou, X.; Li, L.; Li, H.; Zhai, T. 2D Ternary Chalcogenides. *Adv. Opt. Mater.* **2018**, 6 (14), 1800058.
- (20) Jenjeti, R. N.; Kumar, R.; Austeria, M. P.; Sampath, S. Field Effect Transistor Based on Layered NiPS₃. *Sci. Rep.* **2018**, 8 (1), 8586.
- (21) Goossens, D. J. Dipolar Anisotropy in Quasi-2D Honeycomb Antiferromagnet MnPS₃. *Eur. Phys. J. B* **2010**, 78 (3), 305–309.
- (22) Lee, J. U.; Lee, S.; Ryoo, J. H.; Kang, S.; Kim, T. Y.; Kim, P.; Park, C. H.; Park, J. G.; Cheong, H. Ising-Type Magnetic Ordering in Atomically Thin FePS₃. *Nano Lett.* **2016**, 16 (12), 7433–7438.
- (23) Mayorga-Martinez, C. C.; Sofer, Z.; Sedmidubský, D.; Huber, Š.; Eng, A. Y. S.; Pumera, M. Layered Metal Thiophosphite Materials: Magnetic, Electrochemical, and Electronic Properties. *ACS Appl. Mater. Interfaces* **2017**, 9 (14), 12563–12573.
- (24) Zhang, J.; Nie, Y.; Wang, X. guang; Xia, Q. lin; Guo, G. hua. Strain Modulation of Magnetic Properties of Monolayer and Bilayer FePS₃ Antiferromagnet. *J. Magn. Magn. Mater.* **2021**, 525, 167687.
- (25) Kim, T. Y.; Park, C. Magnetic Anisotropy and Magnetic Ordering of Transition-Metal Phosphorus Trisulfides. *Nano Lett.* **2021**, 21, 10114–10121.
- (26) Gibertini, M.; Koperski, M.; Morpurgo, A. F.; Novoselov, K. S. Magnetic 2D Materials and Heterostructures. *Nat. Nanotechnol.* **2019**, 14 (5), 408–419.
- (27) Clement, R. A Novel Route to Intercalation into Layered MnPS₃. *J. Chem. Soc. Chem. Commun.* **1980**, No. 14, 647–648.
- (28) Spodine, E.; Valencia-Gálvez, P.; Manzur, J.; Paredes-García, V.; Pizarro, N.; Bernot, K.; Venegas-Yazigi, D. Optical Properties of Composites Formed by Transition Metal Macrocyclic Complexes Intercalated in Thiophosphate Layered Phases. *Polyhedron* **2012**, 44 (1), 187–193.
- (29) Spodine, E.; Valencia-Gálvez, P.; Fuentealba, P.; Manzur, J.; Ruiz, D.; Venegas-Yazigi, D.; Paredes-García, V.; Cardoso-Gil, R.; Schnelle, W.; Kniep, R. Magnetic Behavior of MnPS₃ Phases Intercalated by [Zn₂L]²⁺ (LH₂: Macrocyclic Ligand Obtained by Condensation of 2-Hydroxy-5-Methyl-1,3-Benzenedicarbaldehyde and 1,2-Diaminobenzene). *J. Solid State Chem.* **2011**, 184 (5), 1129–1134.
- (30) Joy, P. A.; Vasudevan, S. The Intercalation Reaction of Pyridine with Manganese

- Thiophosphate, MnPS_3 . *J. Am. Chem. Soc.* **1992**, *114* (20), 7792–7801.
- (31) Clement, R.; Girerd, J. J.; Morgenstern-Badarau, I. Dramatic Modification of the Magnetic Properties of Lamellar Manganese Trithiophosphonite (MnPS_3) Upon Intercalation. *Inorg. Chem.* **1980**, *19* (9), 2852–2854.
 - (32) Glass, D. E.; Jones, J.-P.; Shevade, A. V.; Bugga, R. V. Transition Metal Phosphorous Trisulfides as Cathode Materials in High Temperatures Batteries. *J. Electrochem. Soc.* **2020**, *167* (11), 110512.
 - (33) Jana, R.; Chowdhury, C.; Datta, A. Transition-Metal Phosphorus Trisulfides and Its Vacancy Defects: Emergence of a New Class of Anode Material for Li-Ion Batteries. *ChemSusChem* **2020**, *13* (15), 3855–3864.
 - (34) Wang, Y.; Zhou, Z.; Wen, T.; Zhou, Y.; Li, N.; Han, F.; Xiao, Y.; Chow, P.; Sun, J.; Pravica, M.; et al. Pressure-Driven Cooperative Spin-Crossover, Large-Volume Collapse, and Semiconductor-to-Metal Transition in Manganese(II) Honeycomb Lattices. *J. Am. Chem. Soc.* **2016**, *138* (48), 15751–15757.
 - (35) Yang, J.; Zhou, Y.; Guo, Q.; Dedkov, Y.; Voloshina, E. Electronic, Magnetic and Optical Properties of MnPX_3 ($X = \text{S}, \text{Se}$) Monolayers with and without Chalcogen Defects: A First-Principles Study. *RSC Adv.* **2019**, *10* (2), 851–864.
 - (36) Murayama, C.; Okabe, M.; Urushihara, D.; Asaka, T.; Fukuda, K.; Isobe, M.; Yamamoto, K.; Matsushita, Y. Crystallographic Features Related to a van Der Waals Coupling in the Layered Chalcogenide FePS_3 . *J. Appl. Phys.* **2016**, *120* (14), 142114.
 - (37) Chu, H.; Roh, C. J.; Island, J. O.; Li, C.; Lee, S.; Chen, J.; Park, J. G.; Young, A. F.; Lee, J. S.; Hsieh, D. Linear Magnetoelectric Phase in Ultrathin MnPS_3 Probed by Optical Second Harmonic Generation. *Phys. Rev. Lett.* **2020**, *124* (2), 27601.
 - (38) Wildes, A. R.; Okamoto, S.; Xiao, D. Search for Nonreciprocal Magnons in MnPS_3 . *Phys. Rev. B* **2021**, *103* (2), 024424.
 - (39) Ju, H.; Jeong, D. G.; Choi, Y. G.; Son, S.; Jung, W. G.; Jung, M. C.; Kang, S.; Han, M. J.; Kim, B. J.; Park, J. G.; et al. Influence of Stacking Disorder on Cross-Plane Thermal Transport Properties in TMPS_3 ($\text{TM} = \text{Mn}, \text{Ni}, \text{Fe}$). *Appl. Phys. Lett.* **2020**, *117* (6), 063103.
 - (40) Coak, M. J.; Jarvis, D. M.; Hamidov, H.; Wildes, A. R.; Paddison, J. A. M.; Liu, C.; Haines, C. R. S.; Dang, N. T.; Kichanov, S. E.; Savenko, B. N.; et al. Emergent Magnetic Phases in Pressure-Tuned van Der Waals Antiferromagnet FePS_3 . *Phys. Rev. X* **2021**, *11* (1), 11024.
 - (41) Björkman, T.; Kurasch, S.; Lehtinen, O.; Kotakoski, J.; Yazyev, O. V.; Srivastava, A.; Skakalova, V.; Smet, J. H.; Kaiser, U.; Krasheninnikov, A. V. Defects in Bilayer Silica and Graphene: Common Trends in Diverse Hexagonal Two-Dimensional Systems. *Sci. Rep.* **2013**, *3*, 3482.
 - (42) Cretu, O.; Komsa, H. P.; Lehtinen, O.; Algara-Siller, G.; Kaiser, U.; Suenaga, K.; Krasheninnikov, A. V. Experimental Observation of Boron Nitride Chains. *ACS Nano* **2014**, *8* (12), 11950–11957.
 - (43) Vasu, K. S.; Prestat, E.; Abraham, J.; Dlx, J.; Kashtiban, R. J.; Beheshtian, J.; Sloan, J.; Carbone, P.; Neek-Amal, M.; Haigh, S. J.; et al. Van Der Waals Pressure and Its Effect on Trapped Interlayer Molecules. *Nat. Commun.* **2016**, *7*, 12168.

- (44) Köster, J.; Ghorbani-Asl, M.; Komsa, H. P.; Lehnert, T.; Kretschmer, S.; Krasheninnikov, A. V.; Kaiser, U. Defect Agglomeration and Electron-Beam-Induced Local-Phase Transformations in Single-Layer MoTe₂. *J. Phys. Chem. C* **2021**, *125* (24), 13601–13609.
- (45) Banhart, F.; Kotakoski, J.; Krasheninnikov, A. V. Structural Defects in Graphene. *ACS Nano* **2011**, *5* (1), 26–41.
- (46) Zhou, W.; Zou, X.; Najmaei, S.; Liu, Z.; Shi, Y.; Kong, J.; Lou, J.; Ajayan, P. M.; Yakobson, B. I.; Idrobo, J. C. Intrinsic Structural Defects in Monolayer Molybdenum Disulfide. *Nano Lett.* **2013**, *13* (6), 2615–2622.
- (47) Susi, T.; Kotakoski, J.; Kepaptsoglou, D.; Mangler, C.; Lovejoy, T. C.; Krivanek, O. L.; Zan, R.; Bangert, U.; Ayala, P.; Meyer, J. C.; et al. Silicon-Carbon Bond Inversions Driven by 60-KeV Electrons in Graphene. *Phys. Rev. Lett.* **2014**, *113* (11), 115501.
- (48) Luo, C.; Wang, C.; Wu, X.; Zhang, J.; Chu, J. In Situ Transmission Electron Microscopy Characterization and Manipulation of Two-Dimensional Layered Materials beyond Graphene. *Small* **2017**, *13* (35), 1604259.
- (49) Lehnert, T.; Ghorbani-Asl, M.; Köster, J.; Lee, Z.; Krasheninnikov, A. V.; Kaiser, U. Electron-Beam-Driven Structure Evolution of Single-Layer MoTe₂ for Quantum Devices. *ACS Appl. Nano Mater.* **2019**, *2* (5), 3262–3270.
- (50) Komsa, H. P.; Kotakoski, J.; Kurasch, S.; Lehtinen, O.; Kaiser, U.; Krasheninnikov, A. V. Two-Dimensional Transition Metal Dichalcogenides under Electron Irradiation: Defect Production and Doping. *Phys. Rev. Lett.* **2012**, *109* (3), 035503.
- (51) Lehnert, T.; Lehtinen, O.; Algara-Siller, G.; Kaiser, U. Electron Radiation Damage Mechanisms in 2D MoSe₂. *Appl. Phys. Lett.* **2017**, *110* (3), 033106.
- (52) Zhang, J.; Yu, Y.; Wang, P.; Luo, C.; Wu, X.; Sun, Z.; Wang, J.; Hu, W. Da; Shen, G. Characterization of Atomic Defects on the Photoluminescence in Two-Dimensional Materials Using Transmission Electron Microscope. *InfoMat* **2019**, *1* (1), 85–97.
- (53) Köster, J.; Liang, B.; Storm, A.; Kaiser, U. Polymer-Assisted TEM Specimen Preparation Method for Oxidation-Sensitive 2D Materials. *Nanotechnology* **2021**, *32* (7), 075704.
- (54) Egerton, R. F. *Electron Energy-Loss Spectroscopy in the Electron Microscope*, 3rd ed.; Springer New York Dordrecht Heidelberg London, 2011.
- (55) Van Aken, P. A.; Liebscher, B.; Styrsa, V. J. Quantitative Determination of Iron Oxidation States in Minerals Using Fe L_{2,3}-Edge Electron Energy-Loss Near-Edge Structure Spectroscopy. *Phys. Chem. Miner.* **1998**, *25*, 323–327.
- (56) Van Aken, P. A.; Liebscher, B. Quantification of Ferrous/Ferric Ratios in Minerals: New Evaluation Schemes of Fe L₂₃ Electron Energy-Loss Near-Edge Spectra. *Phys. Chem. Miner.* **2002**, *29* (3), 188–200.
- (57) Tan, H.; Verbeeck, J.; Abakumov, A.; Tendeloo, G. Van. Ultramicroscopy Oxidation State and Chemical Shift Investigation in Transition Metal Oxides by EELS. *Ultramicroscopy* **2012**, *116*, 24–33.
- (58) Van Aken, P. A.; Styrsa, V. J.; Liebscher, B.; Woodland, A. B.; Redhammer, G. J. Microanalysis of Fe³⁺/ΣFe in Oxide and Silicate Minerals by Investigation of Electron Energy-Loss Near-Edge Structures (ELNES) at the Fe M_{2,3} Edge. *Phys. Chem. Miner.* **1999**, *26* (7), 584–590.

- (59) Garvie, L. A. J.; Craven, A. J. High-Resolution Parallel Electron Energy-Loss Spectroscopy of Mn L_{2,3}-Edges in Inorganic Manganese Compounds. *Phys. Chem. Miner.* **1994**, 21 (4), 191–206.
- (60) Schmid, H. K.; Mader, W. Oxidation States of Mn and Fe in Various Compound Oxide Systems. *Micron* **2006**, 37, 426–432.
- (61) Madsen, J.; Susi, T. The AbTEM Code: Transmission Electron Microscopy from First Principles. *Open Res. Eur.* **2021**, 1, 24.
- (62) De Graef, M. *Introduction to Conventional Transmission Electron Microscopy*; Cambridge University Press, 2003.
- (63) Powell, C. J. Cross Sections for Ionization of Inner-Shell Electrons by Electrons. *Rev. Mod. Phys.* **1976**, 48 (1), 33–47.
- (64) Gorelik, T. E.; Habermehl, S.; Shubin, A. A.; Gruene, T.; Yoshida, K.; Oleynikov, P.; Kaiser, U.; Schmidt, M. U. Crystal Structure of Copper Perchlorophthalocyanine Analysed by 3D Electron Diffraction. *Acta Crystallogr. Sect. B Struct. Sci. Cryst. Eng. Mater.* **2021**, 77, 662–675.
- (65) Palatinus, L.; Brázda, P.; Jelínek, M.; Hrdá, J.; Steciuk, G.; Klementová, M. Specifics of the Data Processing of Precession Electron Diffraction Tomography Data and Their Implementation in the Program PETS2.0. *Acta Crystallogr. Sect. B Struct. Sci. Cryst. Eng. Mater.* **2019**, 75, 512–522.
- (66) Kresse, G.; Furthmüller, J. Efficient Iterative Schemes for Ab Initio Total-Energy Calculations Using a Plane-Wave Basis Set. *Phys. Rev. B* **1996**, 54 (16), 11169–11186.
- (67) Kresse, G.; Furthmüller, J. Efficiency of Ab-Initio Total Energy Calculations for Metals and Semiconductors Using a Plane-Wave Basis Set. *Comput. Mater. Sci.* **1996**, 6 (1), 15–50.
- (68) Perdew, J. P.; Burke, K.; Ernzerhof, M. Generalized Gradient Approximation Made Simple. *Phys. Rev. Lett.* **1996**, 77 (18), 3865–3868.
- (69) Ouvrard, G.; Brec, R.; Rouxel, J. Structural Determination of Some MPS₃ Layered Phases (M = Mn, Fe, Co, Ni and Cd). *Mater. Res. Bull.* **1985**, 20 (10), 1181–1189.
- (70) Malis, T.; Cheng, S. C.; Egerton, R. F. EELS Log-Ratio Technique for Specimen-Thickness Measurement in the TEM. *J. Electron Microsc. Tech.* **1988**, 8 (2), 193–200.
- (71) Meyer, J. C.; Eder, F.; Kurasch, S.; Skakalova, V.; Kotakoski, J.; Park, H. J.; Roth, S.; Chuvilin, A.; Eyhusen, S.; Benner, G.; et al. Accurate Measurement of Electron Beam Induced Displacement Cross Sections for Single-Layer Graphene. *Phys. Rev. Lett.* **2012**, 108 (19), 196102.
- (72) McKinley, W. A.; Feshbach, H. The Coulomb Scattering of Relativistic Electrons by Nuclei. *Phys. Rev. Lett.* **1948**, 74 (12), 1759–1763.
- (73) Mott, N. F. The Scattering of Fast Electrons by Atomic Nuclei. *Proc. R. Soc. London. Ser. A, Contain. Pap. a Math. Phys. Character* **1929**, 124 (794), 425–442.
- (74) Susi, T.; Hofer, C.; Argentero, G.; Leuthner, G. T.; Pennycook, T. J.; Mangler, C.; Meyer, J. C.; Kotakoski, J. Isotope Analysis in the Transmission Electron Microscope. *Nat. Commun.* **2016**, 7, 13040.
- (75) Susi, T.; Meyer, J. C.; Kotakoski, J. Quantifying Transmission Electron Microscopy

- Irradiation Effects Using Two-Dimensional Materials. *Nat. Rev. Phys.* **2019**, 1 (6), 397–405.
- (76) Kretschmer, S.; Lehnert, T.; Kaiser, U.; Krasheninnikov, A. V. Formation of Defects in Two-Dimensional MoS₂ in the Transmission Electron Microscope at Electron Energies below the Knock-on Threshold: The Role of Electronic Excitations. *Nano Lett.* **2020**, 20 (4), 2865–2870.
 - (77) Komsa, H. P.; Krasheninnikov, A. V. Effects of Confinement and Environment on the Electronic Structure and Exciton Binding Energy of MoS₂ from First Principles. *Phys. Rev. B - Condens. Matter Mater. Phys.* **2012**, 86 (24), 241201.
 - (78) Joseph, T.; Ghorbani-Asl, M.; Kvashnin, A. G.; Larionov, K. V.; Popov, Z. I.; Sorokin, P. B.; Krasheninnikov, A. V. Nonstoichiometric Phases of Two-Dimensional Transition-Metal Dichalcogenides: From Chalcogen Vacancies to Pure Metal Membranes. *J. Phys. Chem. Lett.* **2019**, 10 (21), 6492–6498.
 - (79) Hofer, F.; Wilhelm, P. EELS Microanalysis of the Elements Ca to Cu Using M₂₃ Edges. *Ultramicroscopy* **1993**, 49 (1–4), 189–197.
 - (80) Brec, R. Review on Structural and Chemical Properties of Transition Metal Phosphorous Trisulfides MPS₃. *Solid State Ionics* **1986**, 22 (1), 3–30.
 - (81) Wildes, A. R.; Simonet, V.; Ressouche, E.; McIntyre, G. J.; Avdeev, M.; Suard, E.; Kimber, S. A. J.; Lançon, D.; Pepe, G.; Moubaraki, B.; et al. Magnetic Structure of the Quasi-Two-Dimensional Antiferromagnet NiPS₃. *Phys. Rev. B - Condens. Matter Mater. Phys.* **2015**, 92 (22), 224408.
 - (82) Graetz, J.; Ahn, C. C.; Ouyang, H.; Rez, P.; Fultz, B. White Lines and D-Band Occupancy for the 3d Transition-Metal Oxides and Lithium Transition-Metal Oxides. *Phys. Rev. B - Condens. Matter Mater. Phys.* **2004**, 69 (23), 235103.
 - (83) Lau, W. M.; Jin, S.; Wu, X. W.; Ingre, S. In Situ X-Ray Photoelectron Spectroscopic Study of Remote Plasma Enhanced Chemical Vapor Deposition of Silicon Nitride on Sulfide Passivated InP. *J. Vac. Sci. Technol. B Microelectron. Nanom. Struct.* **1990**, 8 (4), 848.
 - (84) Wu, R. J.; Topsakal, M.; Low, T.; Robbins, M. C.; Haratipour, N.; Jeong, J. S.; Wentzcovitch, R. M.; Koester, S. J.; Mkhoyan, K. A. Atomic and Electronic Structure of Exfoliated Black Phosphorus. *J. Vac. Sci. Technol. A Vacuum, Surfaces, Film.* **2015**, 33 (6), 060604.
 - (85) T.K. Dennenwaldt. Electron Energy Loss Spectroscopy of Novel Oxide- and Nitride-Based Nanostructured Materials, Ludwig-Maximilians-Universität München, 2013.
 - (86) Kruse, J.; Leinweber, P.; Eckhardt, K. U.; Godlinski, F.; Hu, Y.; Zuin, L. Phosphorus L_{2,3}-Edge XANES: Overview of Reference Compounds. *J. Synchrotron Radiat.* **2009**, 16 (2), 247–259.

TOC Graphic: